

Diagnosing the representation and causes of the ENSO persistence barrier in CMIP5 simulations

Ben Tian¹ · Hong-Li Ren^{1,2} · Fei-Fei Jin³ · Malte F. Stuecker^{4,5}

Received: 25 September 2018 / Accepted: 8 May 2019 / Published online: 14 May 2019 © Springer-Verlag GmbH Germany, part of Springer Nature 2019

Abstract

In this study, the persistence barrier (PB) of the El Niño–Southern Oscillation (ENSO) phenomenon is investigated using reanalysis data and historical simulations of the Coupled Model Intercomparison Project Phase 5 (CMIP5) models. Both the timing and intensity of the ENSO PB can be quantified using the maximum gradient of autocorrelation decline of Niño sea surface temperature (SST) anomaly indices. Most of the CMIP5 models were found to reasonably reproduce the observed timing of the ENSO PB that typically occurs during the boreal late spring to early summer, and underestimated the PB intensity compared to observations. Furthermore, the PB properties of the Eastern Pacific (EP) ENSO indices were much better represented by the models than those of the Central Pacific (CP) ENSO indices, probably because CP ENSO events are more challenging to simulate than their counterparts. Approximately half of the models can satisfyingly reflect the intensity and timing of PB for indices of EP ENSO and their distinctions from those of the CP ENSO, with a larger uncertainty for the modeled PB timing than intensity. Further diagnosis has revealed the relationship between the ENSO PB intensity and the factors associated with the tropical Pacific background state. The PB intensity exhibits a stronger relationship with the seasonality of the SST amplitude in CP, compared to the SST amplitude, and the strength of seasonal synchronization of EP SST anomalies is highly correlated with the PB intensity. These results suggest that the seasonality of tropical SST variability may fundamentally contribute to the ENSO PB.

Keywords ENSO · Persistence barrier · CMIP5 simulations

1 Introduction

The El Niño-Southern Oscillation (ENSO) is the dominant mode of interannual climate variability and has attracted considerable attention due to its large impacts on global

- ☐ Hong-Li Ren renhl@cma.gov.cn
- ¹ Laboratory for Climate Studies, CMA-NJU Joint Laboratory for Climate Prediction Studies, National Climate Center, China Meteorological Administration, Beijing 100081, China
- Department of Atmospheric Science, School of Environmental Studies, China University of Geoscience, Wuhan 430074, China
- ³ Department of Atmospheric Sciences, University of Hawaii, Honolulu 96822, USA
- Center for Climate Physics, Institute for Basic Science (IBS), Busan, Republic of Korea
- Pusan National University, Busan, Republic of Korea

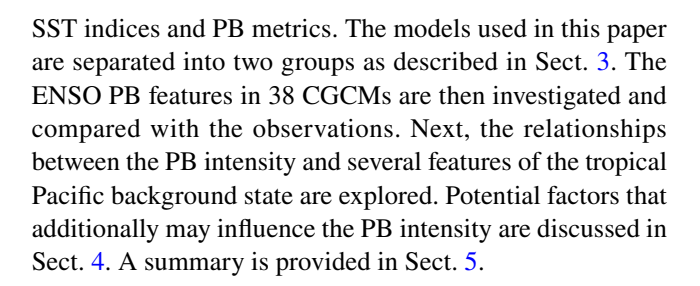
climate (e.g., Rasmusson and Carpenter 1982; Timmermann et al. 2018). Significant progress has been made in understanding and predicting ENSO, and ENSO could now be well predicted 6 months in advance, and probably longer (Barnston et al. 2012; Jin et al. 2008; Latif et al. 1994; Ren et al. 2014; Timmermann et al. 2018; Zhu et al. 2012). Nevertheless, the accuracy of ENSO predictions decreases abruptly for forecasts made before and during boreal spring. This so-called ENSO spring predictability barrier is at least partially caused by seasonal transitions in the monsoon circulation (Webster and Yang 1992), ocean-atmosphere coupling strength variation (Chen et al. 2015; Hu et al. 2011; Larson and Kirtman 2016; Webster 1995; Zebiak and Cane 1987), seasonal change in the signal-to-noise ratio (Barnett et al. 1994; Torrence and Webster 1998; Zheng and Zhu 2010), initial errors of certain specific patterns (Duan et al. 2009; Mu et al. 2007; Tian and Duan 2016b), model biases (Lopez and Kirtman 2015; Zheng and Zhu 2010), seasonality of ocean surface-subsurface connection (Zhu et al. 2015), and westerly wind burst activity (WWB) (Chen



et al. 2015; Larson and Kirtman 2016; Lopez and Kirtman 2015). Importantly, the degree of ENSO seasonal synchronization in the annual cycle seems to affect the spring predictability barrier of ENSO (Levine and McPhaden 2015) and is thought to determine the strength of the ENSO persistence drop-off (Torrence and Webster 1998). The ENSO persistence barrier (PB), which is commonly considered a natural and observable ENSO property, refers to the rapid decline in persistence (lagged autocorrelations) across boreal spring, irrespective of which starting time is chosen. Considering the similarity of basic characteristics between the two phenomena, it is reasonable to hypothesize that the spring predictability barrier in models, including the Coupled Model Intercomparison Project Phase 5 (CMIP5) models, is closely related to the observed ENSO PB; meanwhile, the former may potentially be reduced using improved model initializations (Chen et al. 1995; Mu et al. 2007). Therefore, improving our understanding of the ENSO PB should allow us to identify important dynamical mechanisms that affect operational ENSO predictions.

Previous efforts investigating the ENSO persistence and predictability barrier were mostly conducted using observations and models of limited complexity (e.g., Levine and McPhaden 2015; Mu et al. 2007; Torrence and Webster 1998). In addition, recent findings using the CCSM4 model might be model-dependent (Larson and Kirtman 2016). Therefore, there is ongoing debate regarding the cause of the spring predictability barrier. Moreover, some of the research on the ENSO PB lacks quantitative descriptions. Recently, Ren et al. (2016) proposed measuring the intensity of the ENSO PB using the largest gradient of the autocorrelation decline of Niño indices of the sea surface temperature (SST) anomaly and demonstrated distinct PB features in terms of the two ENSO types (Ashok et al. 2007; Kao and Yu 2009; Kug et al. 2009). Here we combine the aforementioned measures of ENSO PB occurrence timing and intensity to assess PB features within a large group of coupled general circulation models (CGCMs). Exploring the ENSO PB phenomenon and its causes is feasible using this approach due to large number of models contributing to CMIP5. It was previously assumed that the simulation performance of the ENSO PB may be related to the seasonal synchronization of ENSO in these models (Torrence and Webster 1998). Therefore, an improved understanding of the ENSO PB may also enable future model improvement. It is important to note that many of the current generation of climate models fail to simulate the Central Pacific (CP) ENSO events realistically (Ham and Kug 2012; Kim and Yu 2012). Therefore, we use various ENSO indices to explore PBs in distinct SST anomaly (SSTA) regions, which characterize SST variability associated with Eastern Pacific (EP) and CP ENSO, respectively.

The observational data and utilized models are introduced in Sect. 2, together with definitions related to the ENSO



2 Data

Monthly data from 38 CMIP5 models (Taylor et al. 2012) is utilized (see Table 1). Realizing that ENSO PB could experience decadal variability just like other properties of ENSO such as the amplitude and period, we analyze the historical simulations (also referred to as twentieth century simulations) and focus on the most recent 30 years of those experiments (1976–2005), a period of reliable contemporary observations to compare to. Ice and sea surface temperature (HadISST, Rayner 2003) data is obtained for the same time period. The observed ENSO PB characteristics are virtually identical to HadISST when using Extended Reconstructed Sea Surface Temperature V3b (ERSST) monthly data from NCEI/NOAA for our analysis (Smith et al. 2008). We also use two sets of surface wind stress monthly data from NCEP/NCAR Reanalysis 1 between 1976 and 2005 (Kalnay et al.

Table 1 The 38 CMIP5 models (18 models that simulate ENSO PB better are in italics, please see text for details) used in this manuscript

No.	Model abbreviated	No.	Model abbreviated
1	Access1-0	20	GISS-E2-H
2	Access1-3	21	GISS-E2-R
3	BCC-CSM1-1	22	HadCM3
4	BCC-CSM1-1-m	23	HadGEM2-AO
5	CanCM4	24	HadGEM2-CC
6	CanESM2	25	HadGEM2-ES
7	CCSM4	26	INMCM4
8	CESM1-BGC	27	IPSL-CM5A-LR
9	CESM1-CAM5	28	IPSL-CM5A-MR
10	CMCC-CESM	29	IPSL-CM5B-LR
11	CMCC-CM	30	MIROC5
12	CMCC-CMS	31	MIROC-ESM-CHEM
13	CNRM-CM5	32	MIROC-ESM
14	CSIRO-Mk3-6-0	33	MPI-ESM-LR
15	FGOALS-g2	34	MPI-ESM-MR
16	FIO-ESM	35	MPI-ESM-P
17	GFDL-CM3	36	MRI-CGCM3
18	GFDL-ESM2G	37	NorESM1-ME
19	GFDL-ESM2M	38	NorESM1-M



1996) and between 1980 and 2005 from the NCEP-DOE Reanalysis 2 (Kanamitsu et al. 2002).

The Niño3.4, Niño3, and Niño4 indices (defined as SSTA averages over the respective regions) are adopted as measures for ENSO-associated SST anomalies. The Cold-Tongue and Warm-Pool (NiñoCT and NiñoWP, respectively) Niño indices defined by Ren and Jin (2011) are used together with the El Niño Modoki index proposed by Ashok et al. (2007). These different ENSO indices are used to investigate PBs in distinct SSTA regions associated with the two ENSO types. In addition to the aforementioned Niño indices, we utilize the first two SSTA empirical orthogonal functions (EOFs) in the tropical Pacific (30°S–30°N, 110°E–70°W), and their corresponding principal components: Niño-PC1 and Niño-PC2, which provides an additional measure for EP and CP ENSO. All indices are calculated for the 1976–2005 period with the 30-year climatologies and linear trends removed

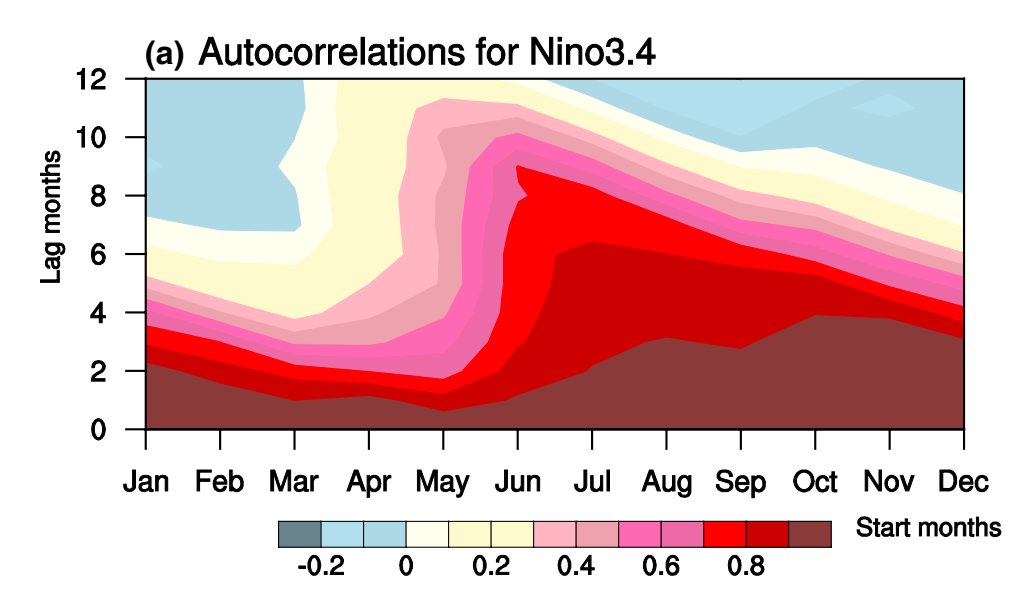
from the SST data. In observation, Niño3, Niño3.4, NiñoCT and Niño-PC1 usually depict EP ENSO better.

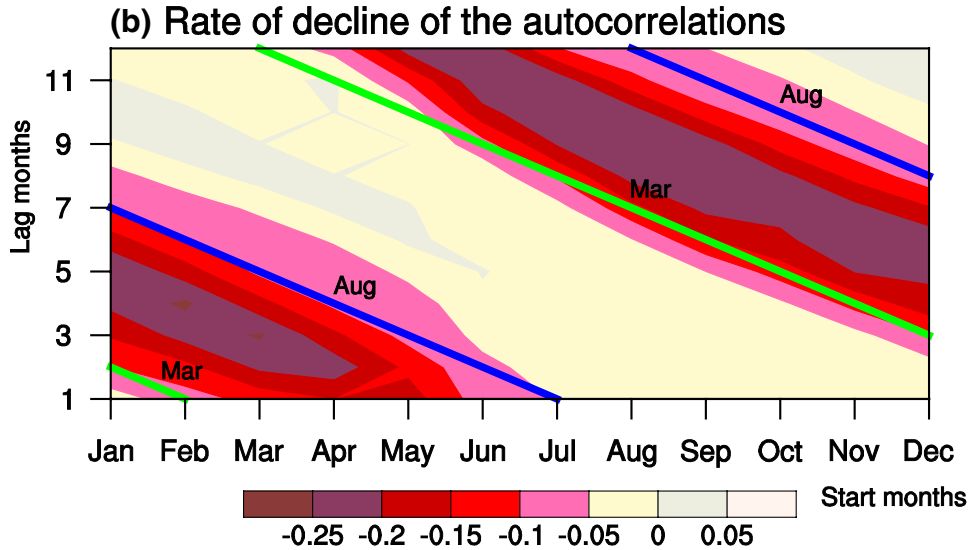
3 ENSO PB in CMIP5 model outputs

3.1 Simulated PB characteristics

The PB is a clear observable feature of the Niño3.4 index. ENSO persistence represented by the autocorrelation of the Niño3.4 index is shown in Fig. 1a. The autocorrelations decline with increasing lag months and exhibit a strong seasonal dependency. Then the autocorrelation decline rate for given ENSO index is expressed by the centered difference of the autocorrelation, i.e., $G_j^i = \left(C_{j+1}^i - C_{j-1}^i\right)/2$. Here i is the initial calendar month, j is the lag month and C_j^i is the

Fig. 1 a Autocorrelations as a function of initial calendar month and lag month for Niño3.4 index (from HadISST), and b decline rate of autocorrelations (month⁻¹) as a function of initial calendar month and lag month for the Niño3.4 index where green and blue lines denote target months of March and August, respectively, in the lag month domain







autocorrelation of the ENSO index for a given start and lag month (see Fig. 1a). Thus, the G_i^i value that results from the centered difference of C_i^i reflects the autocorrelation decline rate for given ENSO index. The maximum decline rate of autocorrelation (nearly all the autocorrelation decline gradients are negative and absolute values reflect the decline rapidity) for the Niño3.4 index (Fig. 1b) occurs primarily in boreal spring and summer, viz., from March to August and is centered around June. In contrast, a weaker loss of persistence is observed for the other target calendar months, which is consistent with previous studies (e.g., Yu and Kao 2007; Ren et al. 2016). Note that decline rate of autocorrelations for the Niño3.4 index could be shown as a function of initial calendar month and lag month as in Fig. 1b, and can also be transformed into Fig. 2 where it is expressed as a function of target calendar month and lag month. So in general, Figs. 1b and 2 present similar information but from different viewpoints. Specifically, PB intensity and timing could be more distinct quantitatively among varied models when they are related to target calendar month. As shown in Fig. 2, the majority of the 38 models reasonably reproduce the observed ENSO PB features, such as PB intensity and PB timing; however, some models show a weaker Niño3.4 PB intensity. To further quantify these characteristics, the 12-lag-month mean (average over the Y-axis in Fig. 2) of the decline rates of the Niño3.4 autocorrelation is plotted as a function of target calendar month (Fig. 3). The 38 models are then classified into two groups based on the following two criteria: (1) whether the two largest Niño3.4 autocorrelation decline rates in Fig. 3 are situated between the target months of April and July as observed, and (2) whether this maximum decline rate reaches a similar value (a value less than -0.15 month^{-1}) as seen in the observations (Fig. 3). The models that satisfy both of these conditions are then included in group A (marked by italics in Table 1: 18 models), and the remainder is placed in group B. Meanwhile, based on the observed ENSO PB pattern (from HADISST) in Fig. 2, the simulations of two groups of models are presented in a Taylor diagram (Fig. 4). Indeed, there is a great contrast between models in group B and the two observational data sets. The subsequent analysis will be conducted following this group classification.

The Niño indices describing the different ENSO types (i.e., EP and CP) exhibit different PB magnitudes in observations (Ren et al. 2016). For each ENSO metric, the PB intensity (PBI) index, which is dependent on the start month, is defined by summing up the rates of autocorrelation decline from March to August within the first 12 lag months, i.e., PBI $^i = -\sum_{k=\mathrm{Mar}}^{\mathrm{Aug}} G_k^i$, where $G_j^i = \left(C_{j+1}^i - C_{j-1}^i\right)/2$ (Ren et al. 2016). Here i is the initial calendar month, j is the lag month and C_j^i is the autocorrelation of the ENSO index for a given start and lag month. The mean of all PBI index values

for 12 initial months of a given Niño index is used to characterize the PB intensity of this Niño index and is termed mPBI. Notice the definition of PBI (as well as mPBI) in Ren et al. (2016) corresponds to generally positive values for PBI, which could help better describe the decline rapidity. In Fig. 5, the PBI index is given as a function of the initial calendar month and only four Niño indices are shown to represent our main points (For ENSO PB of other Niño indices, one could refer to Fig. 6 of a comprehensive collection). In the observations, EP ENSO has a significantly stronger PB than CP ENSO, with Niño3.4 having the largest PBI (Fig. 5). The observed Niño4 index exhibits the strongest PB among those CP ENSO indices, potentially because it captures some EP ENSO variability (Niño3.4 and Niño4 are not orthogonal). To examine the modeled PB intensity, we compared the PBI for different Niño indices between models in terms of the two aforementioned groups and show their composites in Fig. 5. Both the observations and model composites exhibit a similar PB intensity for these ENSO indices; the EP ENSO indices (the left row in Fig. 5) have significantly larger PBIs than the CP ENSO indices, although this is less evident for the models in group B.

As mentioned earlier, the group classifications are based on the model representations of Niño3.4 autocorrelation decline; however, model simulations of all EP ENSO indices in group A, rather than those in group B, have a more similar PB to the parallel observations (Fig. 6). Meanwhile, it is noted that the two model groups perform equally in terms of PB intensity simulation of CP ENSO indices and the PBI indices remain somewhat stronger in group A, compared to the group B models (Fig. 6).

The PB timing for these ENSO indices is another focus of our comparison in addition to the PB intensity. For a given start month, the time when the most rapid autocorrelation decline arises represents the occurrence of ENSO PB for that month, and the mean of all PB occurrence time for the 12 initial months is utilized to represent the PB timing for a given Niño index. In Fig. 7, the PB timing for the 38 models is presented along with relevant observations. As indicated by Ren et al. (2016), the PB in observations generally occurs in boreal late spring-early summer for EP ENSO and in boreal summer for the CP ENSO. Compared to the EP ENSO indices, the observed PB timing is clearly delayed for the CP ENSO indices (the right row in Fig. 7), which can be generally represented by the CMIP5 models but with a large inter-model spread. Compared to the PB intensity in Fig. 5, the PB occurrence time in these models exhibits no clear structure, especially for the CP ENSO indices; however, the group mean does not significantly deviate from the observed features due to the inter-model offset. This conspicuous divergence as well as the departure from the observed ENSO PB timing reflects the unrealistic representation of CP ENSO (including the second EOF of tropical Pacific SSTA) in



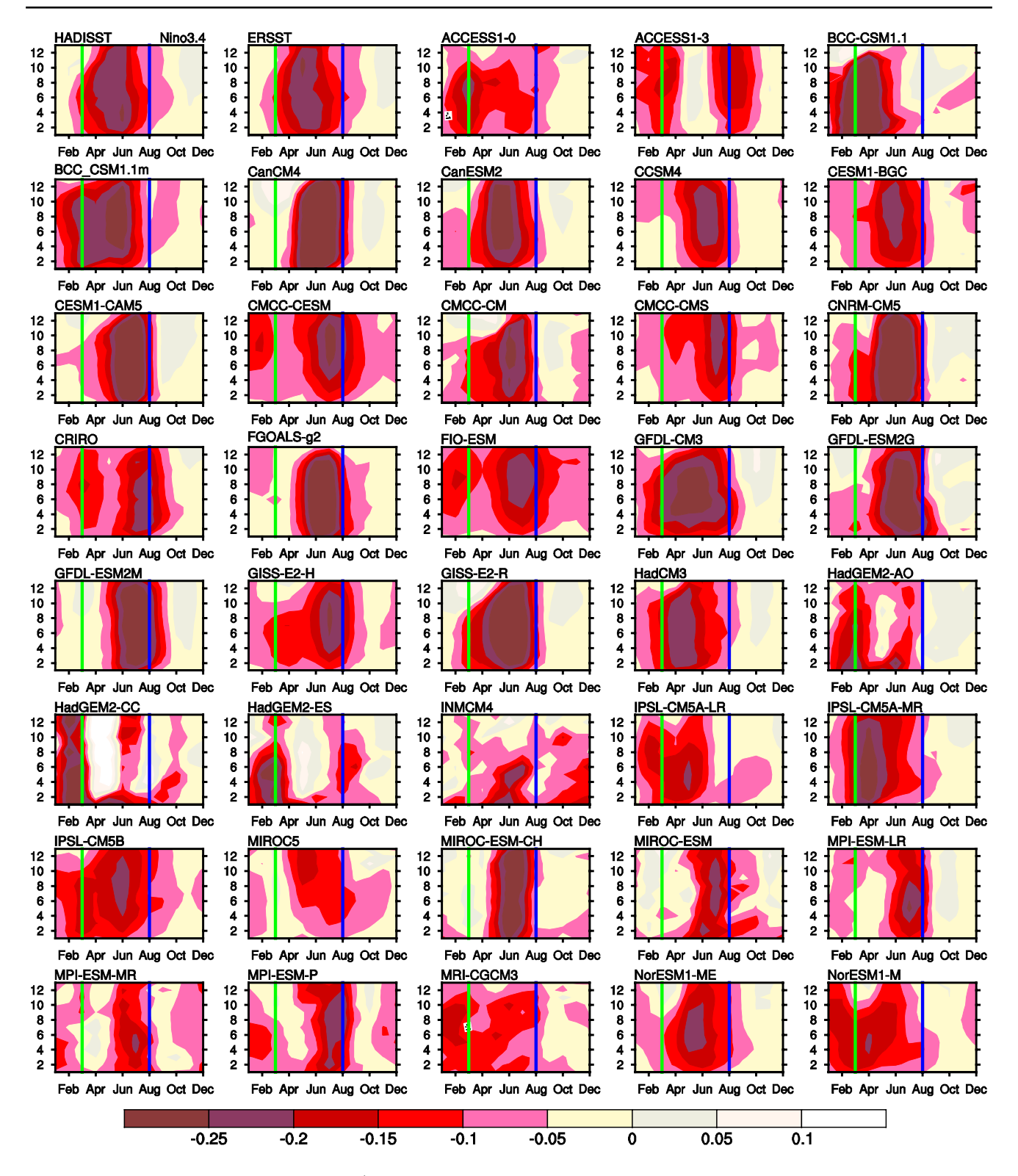


Fig. 2 Decline rates of autocorrelations (month⁻¹) as a function of target calendar month and lag month for the Niño3.4 index among observations (HadISST and ERSST) and the CMIP5 models. Green

and blue lines demonstrate the decline rates of autocorrelation targeting March and August with all the lag months, respectively. Model names are defined in Table 1



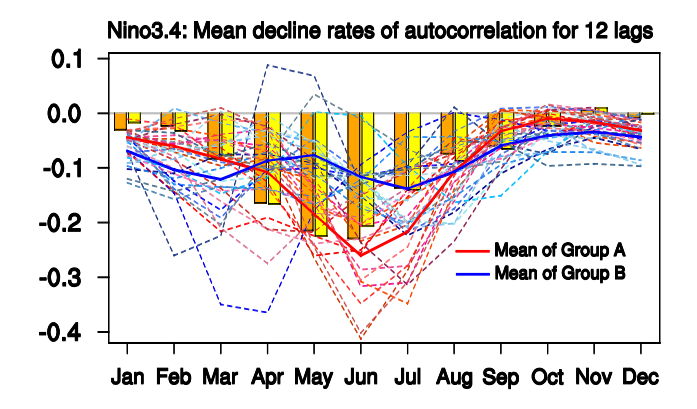


Fig. 3 The average autocorrelation decline rates (month⁻¹) for all 12 lag months as a function of target calendar month for the Niño3.4 index among HADISST (orange bars), ERSST (yellow bars), and CMIP5 model output (dashed lines). The two CMIP5 group means (please see Sect. 3.1 for model classification) highlight the ENSO PB as seen in Fig. 2

current models (see Fig. 6 for other Niño indices). For both the observations and the ensemble mean of group A, the EP ENSO indices generally show a PB occurring in May–June, while the PB timing for the CP ENSO indices occurs about one or 2 months later in June–July. This characteristic is less clear for the ensemble mean of the group B models, which tends to be generally around May–June (Fig. 6). At present, most of the models still have problems simulating CP ENSO

realistically, especially its center location and SST anomaly amplitude (Ham and Kug 2012; Kim and Yu 2012). What we find here further suggests that the simulated PB of EP ENSO rather than CP ENSO could potentially be utilized to distinguish the performance between different models. In this regard, an unrealistic representation of CP ENSO may limit the prediction of CP ENSO as well and thus it may be not suitable to explore whether EP or CP ENSO is more predictable within current models, which will be further discussed in Sect. 5.

3.2 ENSO PBI and its causes

In this section, several aspects of the model background state that may relate to the ENSO PB intensity bias are investigated. It is evident that both in observations and model simulations, the PBs of the EP ENSO indices are much more pronounced compared to those of the CP ENSO indices (e.g., Fig. 6). Given the weaker strength of CP ENSO compared to EP ENSO (Ashok et al. 2007; Kao and Yu 2009; Kug et al. 2009), the obvious question here is whether the PB intensity of a given ENSO index is positively correlated to the amplitude of that index. Here, the standard deviation (STD) is utilized to characterize the amplitude of a certain ENSO index. Here, we focus on the PB intensity of Niño3.4 index only, which is the most commonly used index for monitoring and predicting ENSO.

Fig. 4 Taylor diagram comparing the two groups of CMIP5 model simulations (blue and red dots) and ERSST with the observed ENSO PB pattern (from HADISST) in Fig. 2. Group A consists of 18 models and group B of 20 models. The model numbers are the same as in Table 1. Note that three models in group B are not seen in the diagram as they exhibit negative correlations with the observations

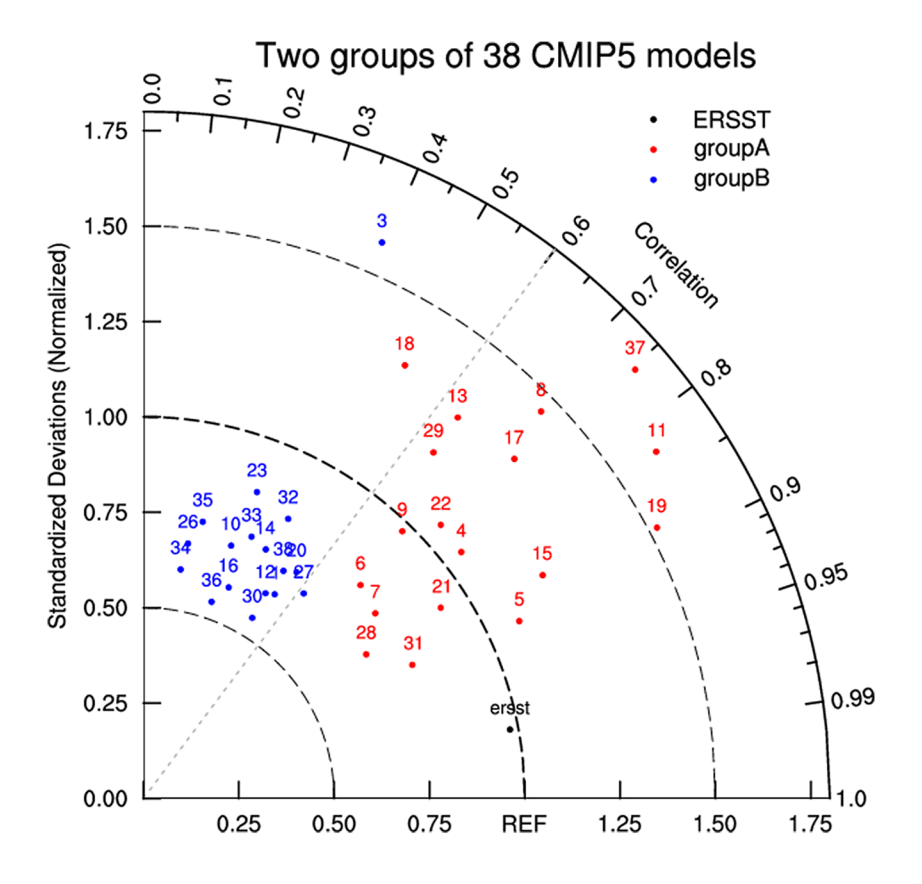
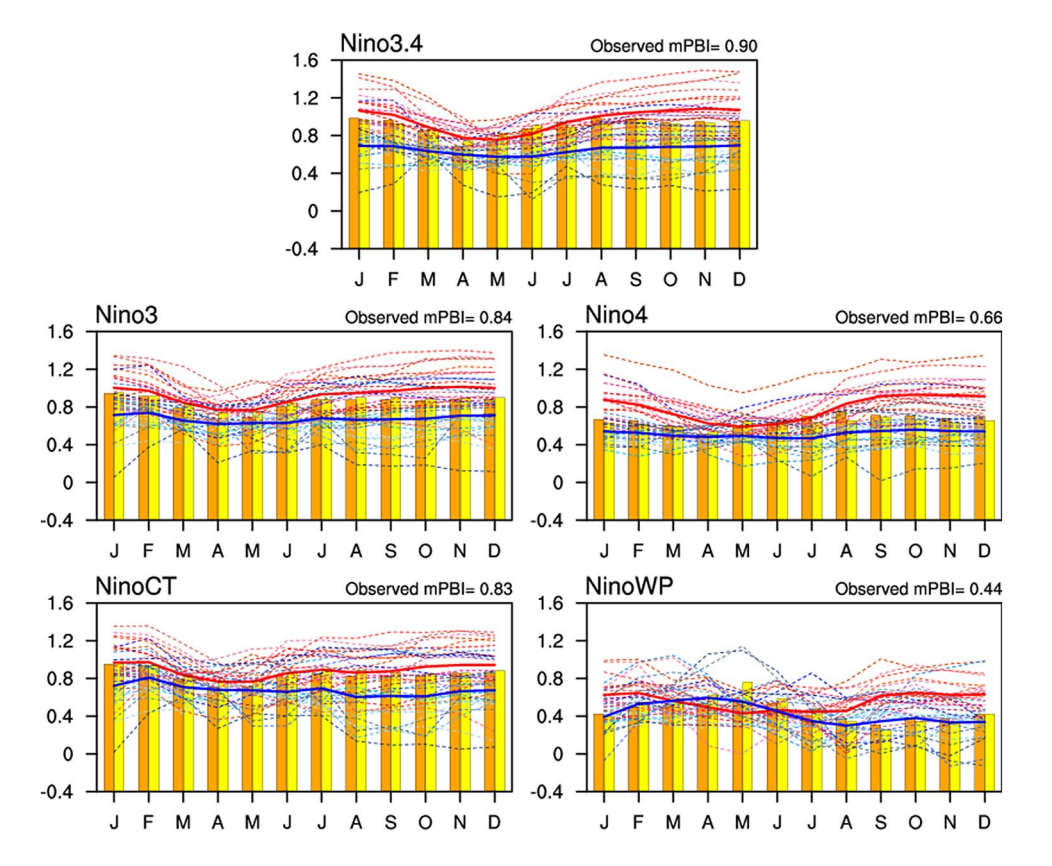




Fig. 5 PBI indices of varied ENSO Niño indices as a function of initial calendar month (month⁻¹), where mPBI denotes the annual mean PBI index of 12 initial calendar months. Observed mPBI in each panel is obtained from HadISST. Orange and yellow bars indicate HadISST and ERSST results, respectively, and red and blue dashed lines indicate models from group A and B, respectively. Solid lines indicate each group's ensemble mean



We calculate 40 STDs for each grid point using the Pacific SSTA observations and 38 model simulations (a sequence with a sample size of 40) with the 30-year climatologies and linear trends removed (see Fig. 8 for an illustration). These 40 STD fields are then used to obtain correlations with Niño3.4 PBI with those 40 samples. Hereinafter, Niño3.4 PBI is expressed by mPBI of the same index. As shown in Figs. 8 and 9, some positive correlations can be seen in the tropical central-eastern Pacific, but these are only statistically significant at the 95% confidence level between SSTA STD and PBI of Niño3.4 in boreal winter (Fig. 9b). We also find that the correlation between amplitude and PBI of the ENSO Niño3.4 is generally only moderate (Fig. 9c, d). Therefore, the amplitude of a certain Niño SST index is only a modest indicator of the PBI of the same index but may not be the key factor.

Previous studies have emphasized the importance of the annual cycle in the tropical Pacific for explaining the ENSO persistence/predictability barrier, and both observational and theoretical evidence have been given to support this hypothesis (e.g., Torrence and Webster 1998; Mu et al. 2007; Levine and McPhaden 2015; Larson and Kirtman 2016). For instance, Webster (1995) explained that the PB occurs during boreal spring when the signal-to-noise ratio in the air—sea coupled system is lowest and the near-equatorial circulation is most easily perturbed by external influences. Therefore, we hypothesize that the seasonality of SSTA

amplitude in the tropical Pacific rather than the SSTA amplitude may play a more important role in influencing ENSO PB intensity. Here, we first explore the relationship between ENSO PB intensity and the seasonality of the SSTA amplitude. The seasonality of the Pacific SSTA STD is defined as follows: $SI_{STD} = Max(STD_{12-month}) - Min(STD_{12-month}),$ where $STD_{12-month}$ represents the monthly standard deviation of SSTA evolution, comprising the 12 values of the 12 calendar months at each grid point for both the observations and models. In this sample of 40, the correlation patterns between SI_{STD} of Pacific SSTA and PBI of Niño3.4 is shown in Fig. 10a. As hypothesized, the ENSO PBI appears to be closely related to the seasonality of SSTA amplitude in the tropical central Pacific which is the common area for the ENSO indices shown in Fig. 10b, c. That is, the stronger seasonality of SSTA amplitude corresponds to an enhanced Niño3.4 PB intensity (Fig. 10d).

Furthermore, it was also suggested that the strength of the PB seems to depend on the degree of ENSO seasonal synchronization (Torrence and Webster 1998), and the latter one may play a key role in the spring predictability barrier of ENSO (Levine and McPhaden 2015). Thus, we further explore whether the PB intensity is associated with the ENSO seasonal synchronization. The ratio between winter (November–January) and spring (March–May) average Niño-3 SST anomalies standard deviations is adopted (Bellenger et al. 2014), which is a measure of the



Fig. 6 Scatterplots of ENSO PBI and PB timing for HadISST (black solid circle), ERSST (gray solid circle), mean of CMIP5 model group A (red solid circle), and mean of CMIP5 model group B (blue solid circle). For a given model (red and blue squares indicate models from group A and B respectively), PBI is expressed by mPBI of each Niño index. For a given month, the time when the most rapid autocorrelation decline arises represents the occurrence of ENSO PB for that start month, and PB timing is the average of PB occurrence time for 12 initial calendar months. Green line in each panel indicates the month of May as the PB timing, and correlations between ENSO PB timing and PBI are shown on top right of each panel

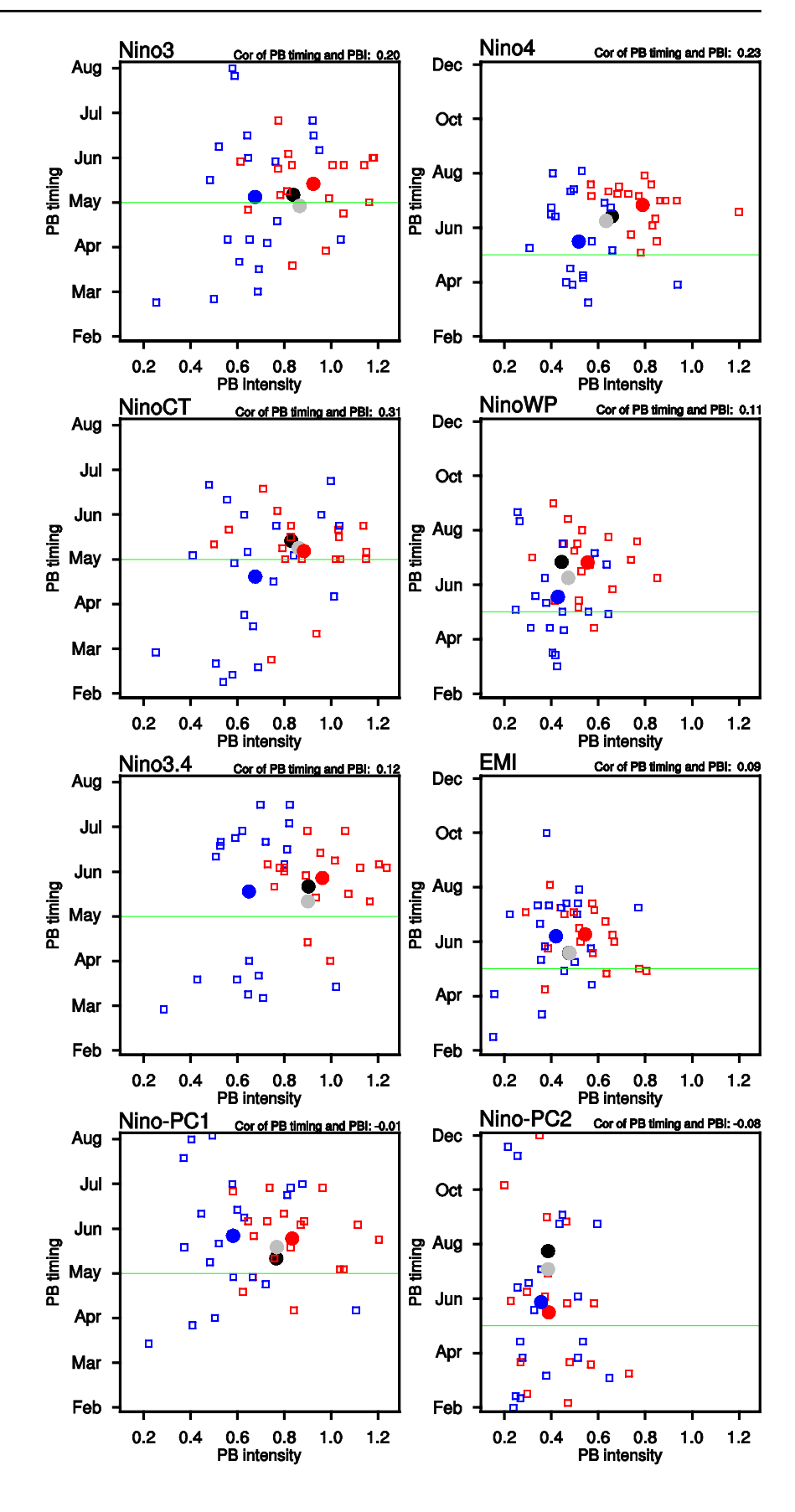
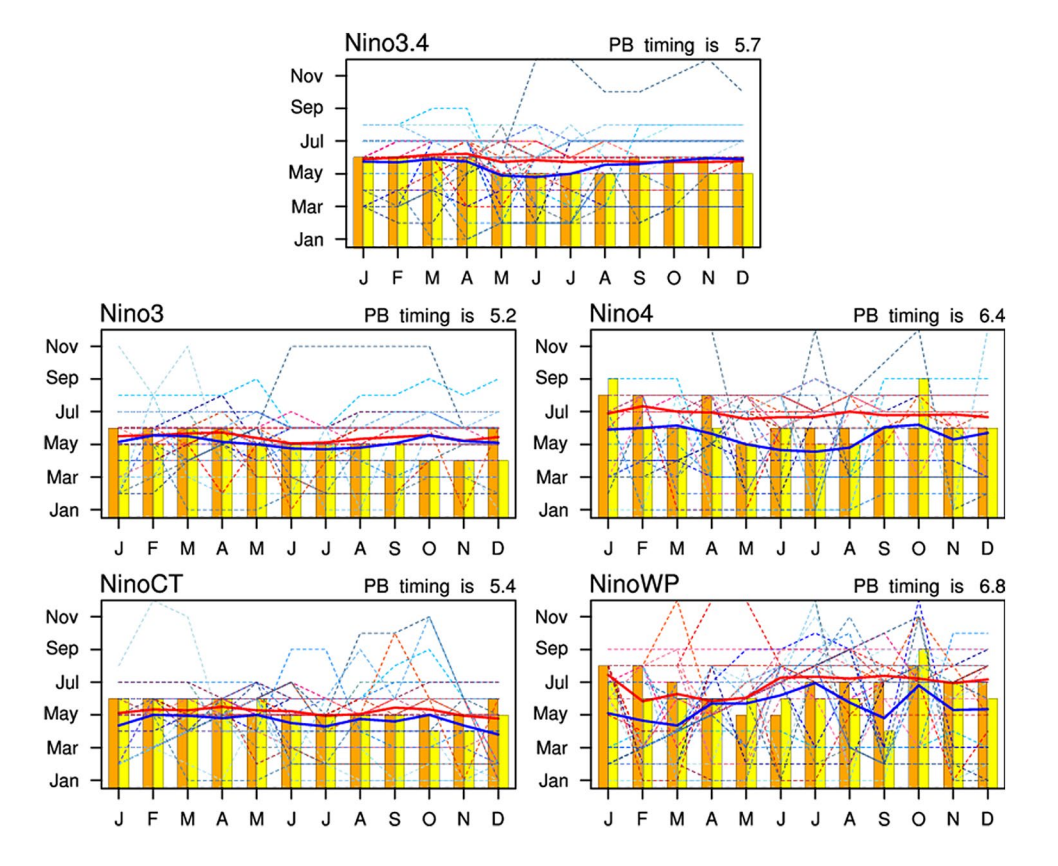




Fig. 7 PB occurrence time for various ENSO indices as a function of the 12 initial calendar months. PB timing is the mean of all PB occurrence time for the 12 initial months and the value (e.g., 1 equals Jan., 2 equals Feb. and so forth) on the top right corner of each panel is obtained from HadISST. Orange and vellow bars indicate HadISST and ERSST results, respectively. Red and blue dashed lines indicate models from group A and B, respectively, with a solid line showing each group's ensemble mean



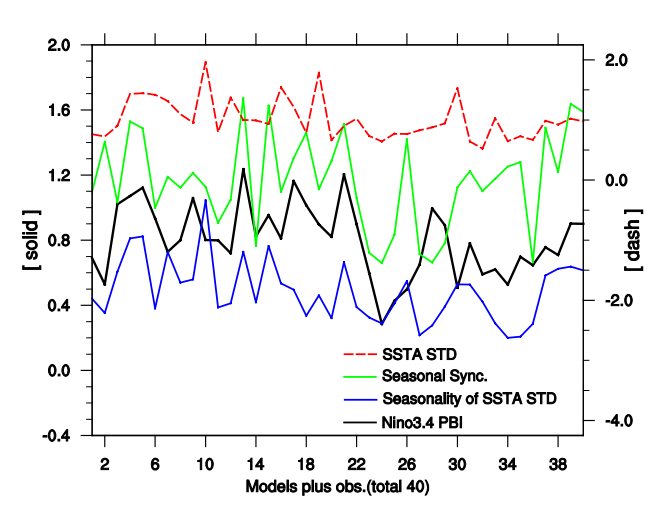
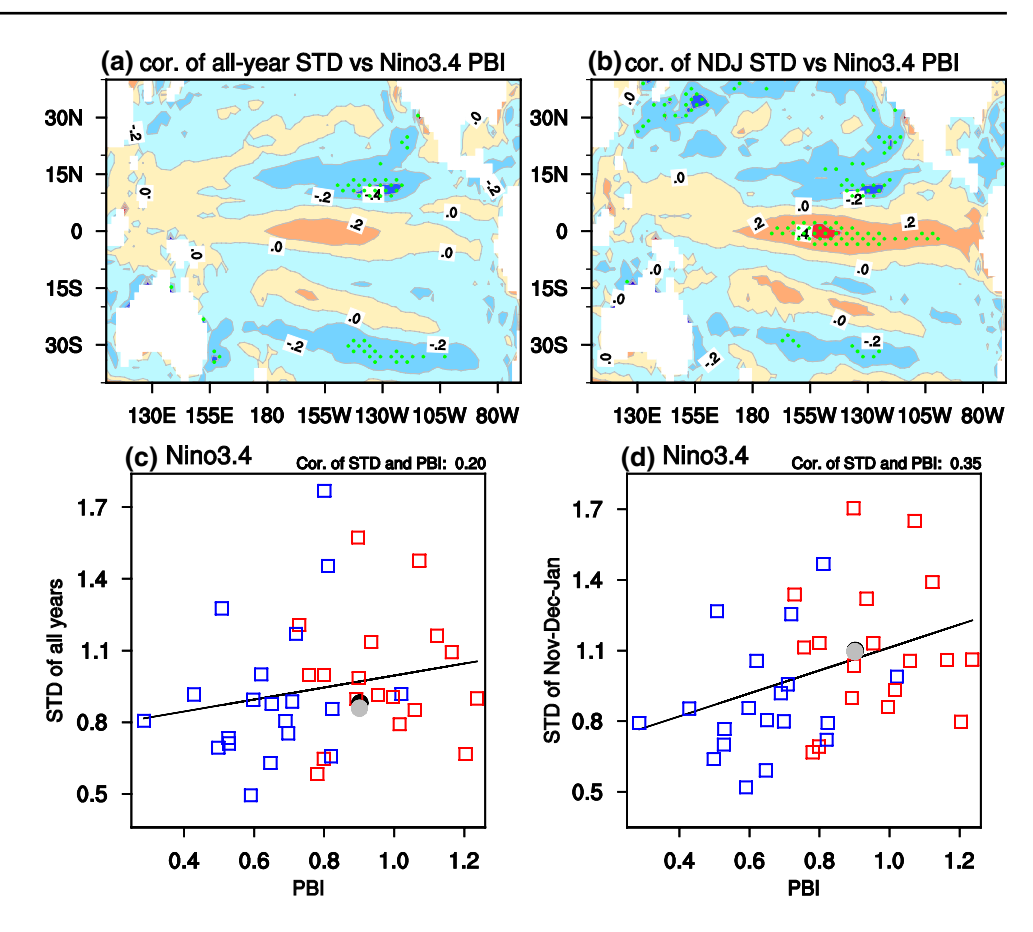


Fig. 8 Schematic diagram of PBIs of Niño3.4 (month⁻¹), SSTA standard deviations (K) of a grid (0°, 160°W), seasonality of SSTA standard deviations (K) of a grid (0°, 160°W), and SST seasonal synchronization strength (dimensionless) of a grid (0°, 120°W) for 40 samples (numbers 1–38 indicate results from the 38 CMIP5 models and numbers 39–40 the two observational data sets, constituting 40 elements in each sequence). The order of models (i.e., from 1 to 38 in each sequence) is the same as in Table 1. Various sequences with a sample size of 40 (like sequences shown here) will be adopted in subsequent correlation analysis

ENSO seasonal synchronization character. Unlike the terminology "phase-locking" used in Bellenger et al. (2014), seasonal synchronization is adopted as it mainly presents the distribution of variance with respect to the annual cycle and better reflects amplitude modulation. This ratio can also be calculated for each grid point individually for the tropical Pacific, referred to as SST seasonal synchronization strength. Statistically significant positive correlations between the PBI and strength of the SST seasonal synchronization can be seen in the tropical eastern Pacific (Fig. 11a). Similarly, in Fig. 11d, the correlation coefficient between the ENSO seasonal synchronization strength and Niño3.4 PBI is relatively high with a correlation of 0.65, denoting significance at the 99% confidence level. These results confirm a close connection between the SST seasonal synchronization and PB intensity of ENSO, as suggested by Torrence and Webster (1998), and provide a reference for understanding model simulations of ENSO persistence. We also find that SST seasonal synchronization is strongest in the eastern Pacific in observations (not shown). This feature can be generally captured by models from group A, however not by the models of group B. Considering the high relevance of the Niño PBI to seasonal synchronization in this area, it may explain why the ENSO PB is stronger in the group A compared to the group B models for a given ENSO index (Figs. 5 and 6).



Fig. 9 Correlation patterns between the standard deviation (STD) of SST anomalies and the Niño3.4 index PBI for 40 samples (two observational data sets and 38 climate models) for the a long term mean and b ENSO mature phase (Nov-Dec-Jan) mean. Green stippling denotes statistical significance at the 95% confidence level. Scatterplots of Niño3.4 PBI and the STD (their correlations are shown on the top right corner of each panel) of the c long term mean, and d Nov-Dec-Jan mean for the same data (black/ gray solid circles indicate HadISST/ERSST, and red/blue squares indicates models from group A/B)



4 Discussion

Thus far, we have assessed the representations of the ENSO PB intensity for multiple Niño indices in CMIP5 model simulations and emphasized the close relationship between it and the tropical Pacific annual cycle (e.g., seasonal synchronization of ENSO). The region that exhibits the strongest relationship between SST seasonal synchronization and PB intensity is located in the eastern Pacific, where SST seasonal synchronization is most pronounced. According to CMIP3 model results, the zonal SST gradient and related zonal wind contribute to the seasonal synchronization of ENSO (Ham et al. 2012). The surface wind stress, which exhibits a strongly seasonally modulated response to Niño3.4 SSTA mainly over the equatorial central Pacific, is an important factor in the seasonal synchronization of ENSO (Ham et al. 2012; Harrison and Vecchi 1999; Stuecker et al. 2013). This implies that the close relationship between ENSO PBI and SSTA that is shown in Fig. 10 may also be seen in atmospheric variables. Thus, we explore the relationship between ENSO PB intensity and the zonal wind stress magnitude seasonality, for which the latter is defined in the same way as the seasonality of SSTA STD. As expected, the region that exhibits the closest relationship is quite similar to the SSTA-related patterns in Fig. 10 with a slightly southward shift towards the location where the strongest air—sea coupling occurs (Ham et al. 2012; Lloyd et al. 2009). Indeed, a weaker relationship is evident between Niño3.4 PBI and the seasonality of surface zonal stress strength among models, with a correlation coefficient of 0.4 that is statistically significant at the 95% confidence level (figure not shown). Thus, the coupling between the mean surface zonal wind and local SST enables the close relationship between ENSO PB intensity and SST seasonality in the tropical central Pacific (Fig. 10), and may even change the way that ENSO seasonal synchronization affects ENSO PB intensity.

One may realize that the two ENSO types are thought to involve different processes but the PB intensity of the two ENSO types is found to closely relate to similar causes. Thus, it is difficult to explain why EP ENSO exhibit a larger PB intensity compared to CP ENSO in this study. The PB of the CP ENSO indices may be more susceptible to the extratropical seasonally varying forcing (e.g., Yu et al. 2010). This stochastic forcing originates from the north Pacific and then influences the tropical central Pacific with a maximum effect in boreal winter according to the Seasonal Footprinting mechanism (Chang et al. 2007; Chiang and Vimont 2004; Vimont et al. 2003). Considering that the tropical central Pacific is the common area where the PB intensity of various Niño indices



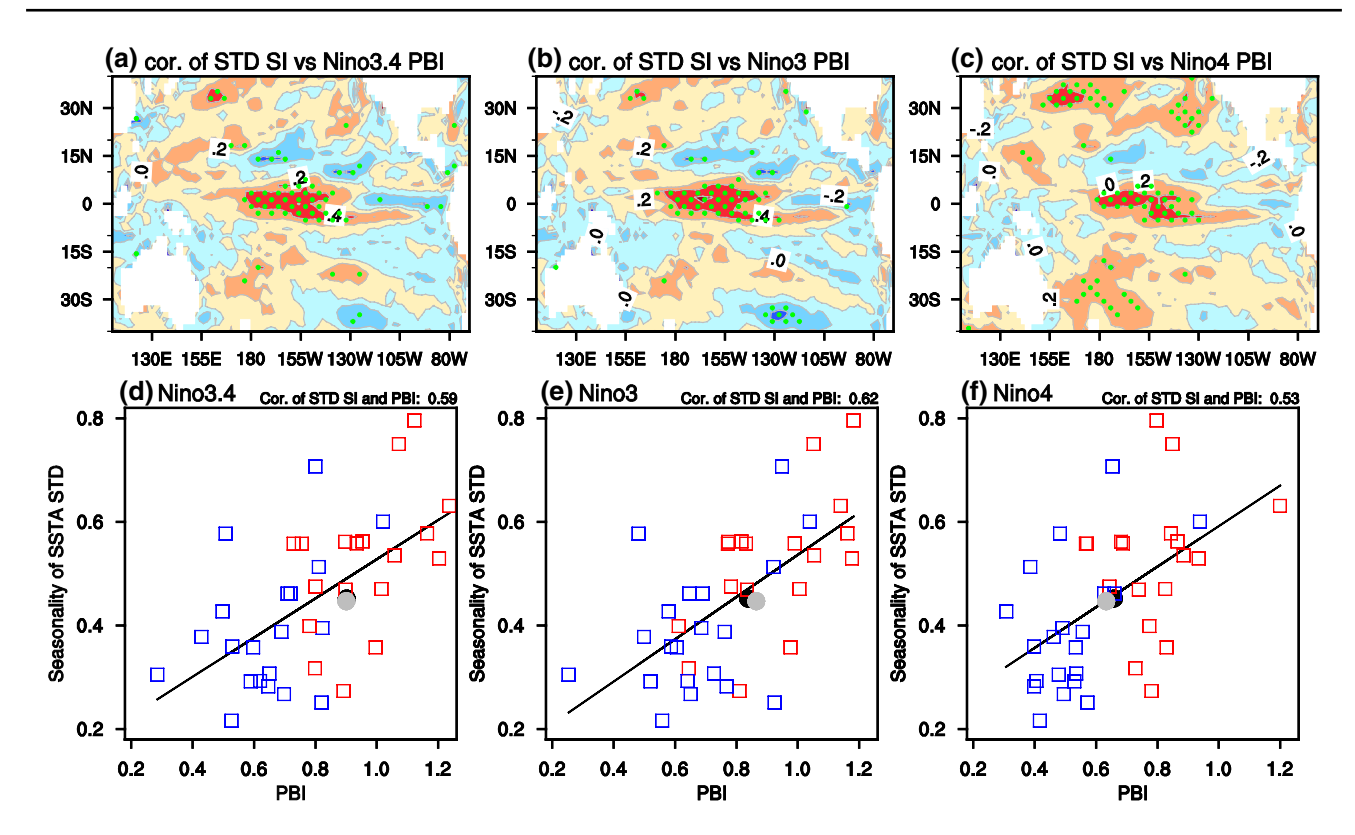


Fig. 10 Correlation patterns between seasonality of SST anomaly standard deviation and the PBI of **a** Niño3.4, **b** Niño3, and **c** Niño4 index for 40 samples (two observational data sets and 38 climate models). Green stippling denotes statistical significance at the 95% confidence level. Scatterplots of ENSO PBI for **d** Niño3.4, **e** Niño3,

and **f** Niño4 and the regional mean (5°S–5°N, 180°–145°W) seasonality of SSTA STD (their correlations are shown on the top right corner of each panel) for the same data (black/gray solid circles indicate HadISST/ERSST, and red/blue squares indicate models from group A/B)

is related to the seasonality of SSTA amplitude, the role of this extratropical process may not result in the PB difference between the two ENSO types directly. As discussed in previous studies (e.g., McPhaden 2012; Yu and Kao 2007), the subsurface ocean temperature over the equatorial Pacific represents a major source for the following SST development in tropical eastern Pacific (EP ENSO events) but with much less effectiveness of thermocline feedbacks in governing the evolution of CP ENSO SST. The equatorial Pacific heat content (also known as warm water volume) anomalies, which exhibit a boreal winter PB that is not further addressed in this study, usually lead the eastern equatorial Pacific SST anomalies by several months (McPhaden 2012; Yu and Kao 2007). Thus, it is reasonable to hypothesize that differing thermocline feedback strength between EP and CP ENSO events might result in a contrast between the PBs of two types of ENSO.

5 Conclusions

Here, we investigated the PB phenomenon for a variety of ENSO indices by comparing historical simulations from 38 CMIP5 models with the observations. Utilizing a metric of

ENSO PBI proposed by Ren et al. (2016), we found that most of the models reasonably reproduced the observed ENSO PB characteristics. Moreover, approximately half of the models also realistically simulated a distinct PBI between CP and EP ENSO indices. The observed PB timing for the ENSO indices can be represented to a lesser degree by the CMIP5 models with a large inter-model spread. Therefore, some indications for distinguishing the two different ENSO types are found in the PB characteristics as simulated by current CMIP5 models.

The relationships between ENSO PBI and several potential physical causes were investigated next. We found a weak relationship between ENSO amplitude and the PBI for various ENSO indices. Instead, the intensity of the PB for different ENSO indices is closely related to the seasonality of the climatological SST amplitude. Furthermore, the intensity of seasonal synchronization of Niño3 SST anomalies to the annual cycle is associated with the ENSO PB intensity. Specifically, the seasonality of the zonal wind stress strength, which constitutes one important part of the tropical coupled system, is thought to influence both the seasonal synchronization of ENSO and the seasonal variation of tropical SSTs. This result provides further evidence that the seasonality



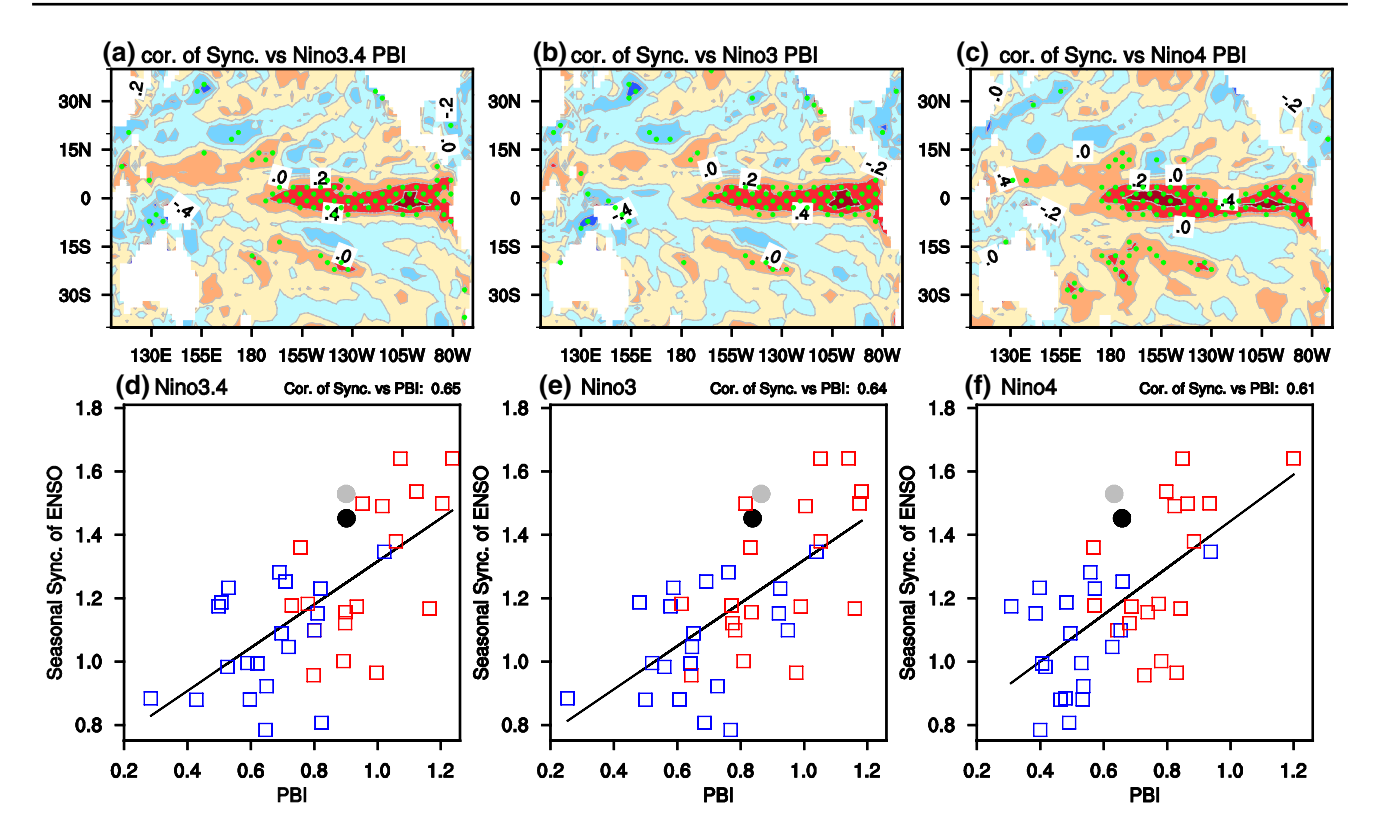


Fig. 11 Correlation patterns between the strength of SST seasonal synchronization (see text for details) and the PBI of **a** Niño3.4, **b** Niño3 and **c** Niño4 index for 40 samples (two observational data sets and 38 climate models). Green stippling denotes statistical significance at the 95% confidence level. Scatterplots of ENSO PBI of

d Niño3.4, **e** Niño3, **f** Niño4 and the strength of ENSO seasonal synchronization (note that their correlations are shown on the top right corner of each panel) for 40 samples (black/gray solid circle indicates HadISST/ERSST, and red/blue squares indicate models from group A/B)

of the tropical Pacific background state is a crucial factor in controlling the ENSO PB. Hence, a better reproduction of ENSO seasonal synchronization might in turn result in a more realistic representation of the ENSO PB in models. Here, only the physical mechanisms related to the ENSO PB intensity were explored, and potential factors controlling the ENSO PB timing difference across models are beyond the scope of this study and may be the subject of future work.

Around half of the CMIP5 models are able to capture the observed discrepancy in PB intensity between the two ENSO types by reproducing a larger PB intensity for EP ENSO than CP ENSO. This suggests that CP ENSO may possess a higher upper limit of predictability in comparison to EP ENSO and could be more predictable by simply setting up autoregression statistical models of the indices. However, it proves difficult to compare the predictability of the two different ENSO types within dynamical prediction models. On one hand, the results here are based on the latest 30 years of CMIP5 historical simulations as well as parallel observations, thus the potential influence of decadal variability (and associated shift in ENSO predictability) on the PB characteristics of the two ENSO types are not considered (McPhaden 2012; Zhu et al. 2015). On the other hand, simulating and predicting CP ENSO, in contrast to

EP ENSO, remains a large challenge. Considerable model drift seems to limit the ability to simulate/predict CP ENSO and the differences between the two types of ENSO (Duan et al. 2014; Hendon et al. 2009; Tian and Duan 2016a). Therefore, an improved understanding of the mechanisms responsible for the two different ENSO types and reduction of model mean state and seasonal cycle biases might open the gates for a more conclusive study of the processes that are responsible for the different PB characteristics, and lead to a more appropriate analysis of predictability of two types of ENSO.

Acknowledgements This work was jointly supported by the National Key Research and Development Program on monitoring, Early Warning and Prevention of Major Natural Disaster (2018YFC1506000), the China National Science Foundation project (41606019 and 41706016), the China Scholarship Council (CSC) State Scholarship Fund, and the Institute for Basic Science (Project code IBS-R028-D1).

References

Ashok K, Behera SK, Rao SA, Weng H, Yamagata T (2007) El Niño Modoki and its possible teleconnection. J Geophys Res. https://doi.org/10.1029/2006JC003798



- Barnett TP et al (1994) Forecasting global ENSO-related climate anomalies. Tellus A 46:381–397
- Barnston AG, Tippett MK, L'Heureux ML, Li S, DeWitt DG (2012) Skill of real-time seasonal ENSO model predictions during 2002–11: is our capability increasing? B Am Meteorol Soc 93:631–651. https://doi.org/10.1175/bams-d-11-00111.1
- Bellenger H, Guilyardi E, Leloup J, Lengaigne M, Vialard J (2014) ENSO representation in climate models: from CMIP3 to CMIP5. Clim Dyn 42:1999–2018. https://doi.org/10.1007/s00382-013-1783-z
- Chang P et al (2007) Pacific meridional mode and El Niño-Southern Oscillation. Geophys Res Lett 34:130–144. https://doi.org/10.1029/2007gl030302
- Chen D, Zebiak SE, Busalacchi AJ, Cane MA (1995) An improved procedure for El Nino forecasting: implications for predictability. Science 269:1699–1702
- Chen D et al (2015) Strong influence of westerly wind bursts on El Niño diversity. Nat Geosci 8:339–345. https://doi.org/10.1038/ngeo2399
- Chiang JCH, Vimont DJ (2004) Analogous Pacific and Atlantic meridional modes of tropical atmosphere–ocean variability. J Clim 17:4143–4158
- Duan W, Liu X, Zhu K, Mu M (2009) Exploring the initial errors that cause a significant "spring predictability barrier" for El Niño events. J Geophys Res 114:C04022. https://doi.org/10.1029/2008jc004925
- Duan W, Tian B, Xu H (2014) Simulations of two types of El Niño events by an optimal forcing vector approach. Clim Dyn 43:1677–1692. https://doi.org/10.1007/s00382-013-1993-4
- Ham Y-G, Kug J-S (2012) How well do current climate models simulate two types of El Nino? Clim Dyn 39:383–398. https://doi.org/10.1007/s00382-011-1157-3
- Ham Y-G, Kug J-S, Kim D, Kim Y-H, Kim D-H (2012) What controls phase-locking of ENSO to boreal winter in coupled GCMs? Clim Dyn 40:1551–1568. https://doi.org/10.1007/s00382-012-1420-2
- Harrison DE, Vecchi GA (1999) On the termination of El Niño. Geophys Res Lett 26:1593–1596. https://doi.org/10.1029/1999gl9003 16
- Hendon HH, Lim E, Wang G, Alves O, Hudson D (2009) Prospects for predicting two flavors of El Niño. Geophys Res Lett. https://doi. org/10.1029/2009g1040100
- Hu Z-Z, Kumar A, Jha B, Wang W, Huang B, Huang B (2011) An analysis of warm pool and cold tongue El Niños: air–sea coupling processes, global influences, and recent trends. Clim Dyn 38:2017–2035. https://doi.org/10.1007/s00382-011-1224-9
- Jin EK et al (2008) Current status of ENSO prediction skill in coupled ocean-atmosphere models. Clim Dyn 31:647-664. https://doi. org/10.1007/s00382-008-0397-3
- Kalnay E et al (1996) The NCEP/NCAR 40-year reanalysis project B. Am Meteorol Soc 77:437–471
- Kanamitsu M, Ebisuzaki W, Woollen J, Yang S, Hnilo JJ, Fiorino M, Potter GL (2002) NCEP-DOE AMIP-II Reanalysis (R-2) B. Am Meteorol Soc 83:1631–1643. https://doi.org/10.1175/bams-83-11
- Kao H-Y, Yu J-Y (2009) Contrasting Eastern-Pacific and Central-Pacific types of ENSO. J Clim 22(3):615–632. https://doi.org/10.1175/2008JCLI2309.1
- Kim ST, Yu J-Y (2012) The two types of ENSO in CMIP5 models. Geophys Res Lett 39:221–228. https://doi.org/10.1029/2012g 1052006
- Kug J-S, Jin F-F, An SI (2009) Two types of El Niño events: cold tongue El Niño and warm pool El Niño. J Clim 22(6):1499–1515. https://doi.org/10.1175/2008JCLI2624.1
- Larson SM, Kirtman BP (2016) Drivers of coupled model ENSO error dynamics and the spring predictability barrier. Clim Dyn 48:3631–3644. https://doi.org/10.1007/s00382-016-3290-5

- Latif M et al (1994) A review of ENSO prediction studies. Clim Dyn 9:167–179
- Levine AFZ, McPhaden MJ (2015) The annual cycle in ENSO growth rate as a cause of the spring predictability barrier. Geophys Res Lett 42:5034–5041. https://doi.org/10.1002/2015gl064309
- Lloyd J, Guilyardi E, Weller H, Slingo J (2009) The role of atmosphere feedbacks during ENSO in the CMIP3 models. Atmos Sci Lett 10:170–176. https://doi.org/10.1002/asl.227
- Lopez H, Kirtman BP (2015) WWBs, ENSO predictability, the spring barrier and extreme events. J Geophys Res Atmos 119:10114–10138. https://doi.org/10.1002/2014jd021908
- McPhaden MJ (2012) A 21st century shift in the relationship between ENSO SST and warm water volume anomalies. Geophys Res Lett. https://doi.org/10.1029/2012gl051826
- Mu M, Xu H, Duan W (2007) A kind of initial errors related to "spring predictability barrier" for El Niño events in Zebiak-Cane model. Geophys Res Lett 34:L03709. https://doi.org/10.1029/2006gl0274
- Rasmusson EM, Carpenter TH (1982) Variations in tropical sea surface temperature and surface wind fields associated with the Southern Oscillation/El Nino. Mon Weather Rev 110:354–384
- Rayner NA (2003) Global analyses of sea surface temperature, sea ice, and night marine air temperature since the late nineteenth century. J Geophys Res 108:1063–1082. https://doi.org/10.1029/2002j d002670
- Ren HL, Jin FF (2011) Nino indices for two types of ENSO. Geophys Res Lett 38:L04704. https://doi.org/10.1029/2010gl046031
- Ren HL, Liu Y, Jin FF, Yan YP, Liu XW (2014) Application of the analogue-based correction of errors method in ENSO prediction. Atmos Ocean Sci Lett 7:157–161. https://doi.org/10.3878/j.issn.1674-2834.13.0080
- Ren H-L, Jin F-F, Tian B, Scaife AA (2016) Distinct persistence barriers in two types of ENSO. Geophys Res Lett 43:10973–10979. https://doi.org/10.1002/2016gl071015
- Smith TM, Reynolds RW, Peterson TC, Lawrimore J (2008) Improvements to NOAA's historical merged land–ocean surface temperature analysis (1880–2006). J Clim 21:2283–2296. https://doi.org/10.1175/2007jcli2100.1
- Stuecker MF, Timmermann A, Jin FF, McGregor S, Ren HL (2013) A combination mode of the annual cycle and the El Nino/Southern Oscillation. Nat Geosci 6:540–544. https://doi.org/10.1038/ NGEO1826
- Taylor KE, Stouffer RJ, Meehl GA (2012) An overview of CMIP5 and the experiment design. B Am Meteorol Soc 93:485–498. https://doi.org/10.1175/bams-d-11-00094.1
- Tian B, Duan W (2016a) Comparison of constant and time-variant optimal forcing approaches in El Niño simulations by using the Zebiak-Cane model. Adv Atmos Sci 33:685–694. https://doi. org/10.1007/s00376-015-5174-8
- Tian B, Duan W (2016b) Comparison of the initial errors most likely to cause a spring predictability barrier for two types of El Niño events. Clim Dyn 47:779–792. https://doi.org/10.1007/s0038 2-015-2870-0
- Timmermann A et al (2018) El Nino-Southern Oscillation complexity. Nature 559:535–545. https://doi.org/10.1038/s41586-018-0252-6
- Torrence C, Webster PJ (1998) The annual cycle of persistence in the El Nino/Southern Oscillation. Q J R Meteorol Soc 124:1985–2004
- Vimont DJ, Wallace JM, Battisti DS (2003) The seasonal footprinting mechanism in the Pacific: implications for ENSO. J Clim 16:2668–2675
- Webster PJ (1995) The annual cycle and the predictability of the tropical coupled ocean-atmosphere system. Meteorol Atmos Phys 56:33–55
- Webster PJ, Yang S (1992) Monsoon and ENSO: selectively interactive systems. Q J R Meteorol Soc 118:877–926



Yu J-Y, Kao H-Y (2007) Decadal changes of ENSO persistence barrier in SST and ocean heat content indices: 1958–2001. J Geophys Res Atmos 112:125–138. https://doi.org/10.1029/2006jd007654

- Yu J-Y, Kao H-Y, Lee T (2010) Subtropics-related interannual sea surface temperature variability in the central equatorial pacific. J Clim 23:2869–2884. https://doi.org/10.1175/2010jcli3171.1
- Zebiak SE, Cane MA (1987) A model El Nino-Southern oscillation. Mon Weather Rev 115:2262–2278
- Zheng F, Zhu J (2010) Spring predictability barrier of ENSO events from the perspective of an ensemble prediction system. Glob Planet Change 72:108–117. https://doi.org/10.1016/j.gloplacha.2010.01.021
- Zhu J, Huang B, Marx L, Kinter JL, Balmaseda MA, Zhang R-H, Hu Z-Z (2012) Ensemble ENSO hindcasts initialized from

- multiple ocean analyses. Geophys Res Lett 39:L09602. https://doi.org/10.1029/2012gl051503
- Zhu JS, Kumar A, Huang BH (2015) The relationship between thermocline depth and SST anomalies in the eastern equatorial Pacific: seasonality and decadal variations. Geophys Res Lett 42:4507–4515. https://doi.org/10.1002/2015GL064220

Publisher's Note Springer Nature remains neutral with regard to jurisdictional claims in published maps and institutional affiliations.

